Near-Surface Currents in DeSoto Canyon (1997–99): Comparison of Current Meters, Satellite Observation, and Model Simulation

DONG-PING WANG

Marine Sciences Research Center, State University of New York at Stony Brook, Stony Brook, New York

LIE-YAUW OEY AND TAL EZER

Program in Atmospheric and Oceanic Sciences, Princeton University, Princeton, New Jersey

PETER HAMILTON

Science Applications International Corporation, Raleigh, North Carolina

4 February 2002 and 3 August 2002

ABSTRACT

This study evaluates a data-assimilated model simulation of near-surface circulation in DeSoto Canyon (DSC), Gulf of Mexico, with emphasis on analyzing moored current-meter observations and comparing them with satellite data and model results. The study period is for two years from April 1997 to April 1999. The model results are from a high-resolution Gulf of Mexico model forced by analyzed wind and surface heat flux. Two types of data are used to deduce near-surface circulation: moored current meters at 13 locations in the DSC, and satellite sea level anomaly. The moored currents are mapped through multivariate objective analysis to produce surface currents and surface geopotentials, against which satellite- and model-derived sea surface heights and geostrophic currents are compared. Coupled patterns between the observations, model results, and satellite data are obtained using the singular value decomposition (SVD) analysis. There are two dominant modes: a ''single-eddy'' mode, in which currents are concentrated at the foot of the canyon, and an ''eddy-pair'' mode, in which one eddy is at the foot of the canyon and the other, a counterrotating eddy, is over the head of canyon. Mode 1 appears to be associated with the mesoscale eddy traveling around the Loop Current crest and trough, and mode 2 is associated with the intrusion of Loop Current crest and trough over the west Florida shelf. The observed and model currents are in good agreement about the means and variances. The model currents also appear to be well constrained by the steep topography. However, the model velocity field contains only the first mode. The satellite-derived velocity field, on the other hand, contains both the first and second modes; though, the satellite field does not adequately resolve the velocity structures over the slope.

1. Introduction

The shelfbreak and slope regions present perhaps the most challenging task for coastal ocean prediction experiments. These regions are under both shelf (e.g., wind and buoyancy-driven) and open-ocean influences. The open-ocean influences, in particular, are difficult to simulate. They typically are due to chaotic mesoscale (~10 to 100 km) eddies whose time-dependent behaviors (with wide-ranging timescales from days and weeks to months) cannot be predetermined and whose spatial structures are poorly resolved by satellite remote sensing. The DeSoto Canyon (DSC) in the northeast gulf is such an example (Fig. 1). The region is sufficiently removed from direct influence of the Loop Current (LC) and Loop Current eddies (LCE), except perhaps in rare occasions when the LC and LCE extrude sufficiently northward (Vukovich et al. 1979; Huh et al. 1981; Wiseman and Dinnel 1988). On the other hand, satellite sea surface temperatures (SST) often reveal complex mesoscale eddy-like structures. In particular, cyclonic eddies, or Loop Current frontal eddies, are frequently found traveling around the periphery of the LC and LCE (Vukovich and Maul 1985). The origin of these eddies is not well understood. Most likely, they are spawned from the LC or LCE through instability and/or eddy-cascade processes. Evidence suggests that the LC frontal eddies may start at the Yucatan Channel and grow in

Corresponding author address: Dr. Lie-Yauw Oey, Princeton University, Forrestal Campus, Program in Atmospheric and Oceanic Sciences, Sayre Hall, Princeton, NJ 08544.
E-mail: lyo@princeton.edu

size as they propagate toward the northern section of the LC (Vukovich 1988).

Previous model studies of the northeast Gulf of Mexico have focused on the direct wind forcing in the absence of LC and LCE (Li and Weisberg 1999; Yuan 2002). Hetland et al. (1999) though has suggested that the impact of LC could spread along the shelf edge, inducing a southward jet along the edge of the west Florida shelf. Their result is consistent with Oey (1996), who found evidence for eddy-induced shelf edge mean currents. Unlike the synoptic wind forcing that lasts for only few days, eddies could stall on the shelf edge over a long period of time (several months to a year), and can have major impacts on the mean circulation. On the other hand, despite circumstantial evidence, direct verification of predicted eddy-induced shelf currents is difficult. The eddy process is fundamentally non-deterministic, and the model generated LC or LCE is not expected to match the time history of the observations. Verification of the Gulf of Mexico model eddy simulation has been limited to the eddy statistics, such as eddy shedding periods and eddy sizes and transports (Oey 1996).

For prediction of shelf edge currents in DSC it is essential that model must be able to realistically represent the LC and LCE and somehow imitate the indirect effects of frontal eddies. Obviously, there is no simple solution to such a complex problem. In this study, we present comparisons of the results from a high resolution ocean prediction experiment with data from a comprehensive network of moored current meter observations. An ocean prediction system, in general, has three basic components: an observational network, a dynamical model, and a data assimilation scheme. In the Gulf of Mexico, satellite remote sensing of sea level anomaly (SLA) and SST provides the only basin-wide observational network. The dynamical model used in this study is a high-resolution three-dimensional Gulf of Mexico model based on the Princeton Ocean Model (POM). The data assimilation scheme follows the classical approach of Mellor and Ezer (1991). The complete model study considers various scenarios of data assimilation and atmospheric forcing (L.-Y. Oey et al. 2002, unpublished manuscript). In this study we use the results from a model experiment (''the complete case''), which assimilates both satellite SST and SLA and is forced by actual wind and surface heat flux. We compare the near-surface currents and sea surface heights derived from the model simulation, current meters, and satellite altimetry data. The study period is over two years, covering several major eddy events.

This study presents the first direct verification of model experiments of eddy-induced shelfbreak and slope circulation in the Gulf of Mexico. As there probably has not been a comparable study done anywhere on the U.S. continental margin, this study offers a rare opportunity to evaluate the soundness of assimilating satellite data to solve the complex problem of coastal prediction over shelfbreak and slope. At present, satellite is the only ''permanent'' basin-wide ocean observation network. While the utility of satellite altimeter in mapping eddies in the open ocean has long been established, relatively little has been explored on assimilating altimeter data on the shelf edge. This study, with the DSC as an example, is a first major step toward a better formulation of ocean prediction systems for shelf break and slope regions.

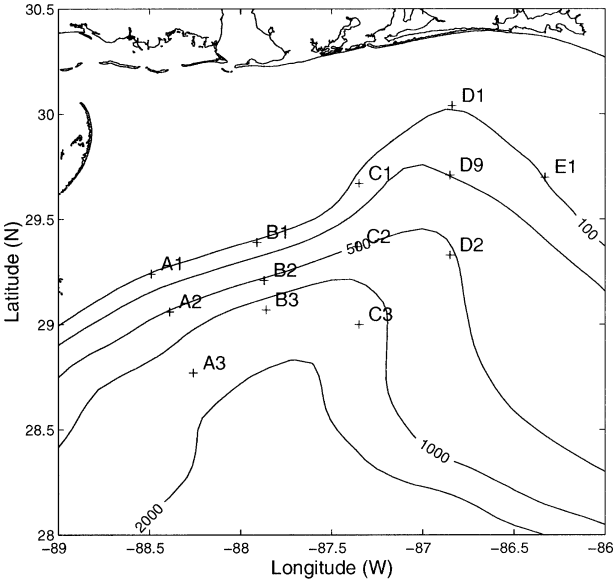

FIG. 1. DeSoto Canyon study area in the northeastern Gulf of Mexico. The current-meter mooring locations are marked.

2. Current meter observations

Current meter data were collected by Science Application International Corporation (SAIC) as part of the DeSoto Canyon Eddy Intrusion Study sponsored by the Minerals Management Service (SAIC 2000). A total of 13 current meter moorings were deployed in the DSC. The moorings were located at 100 m (A1, B1, C1, D1, and E1), 200 m (D9), 500 m (A2, B2, C2, and D2), and 1300 m (A3, B3, and C3). The mooring locations are marked in Fig. 1. On each mooring, except D9, an upward-looking RD Instruments (RDI) Workhorse acoustic Doppler Current Profiler (ADCP) was deployed at 80–90-m depth, and on D9, a 150-kHz RDI Narrowband ADCP was deployed at 180 m. The study period is between April 1997 and April 1999. In all moorings except B1, the record is complete with few minor data gaps. On B1, only the first-year (April 1997 to April 1998) record is available. Preliminary analysis of ADCP velocity profiles found no significant velocity shears in the upper water column at low frequencies. For convenience, near-surface currents are defined as the ADCP currents at 20 m.

The observed currents are lowpass filtered to produce

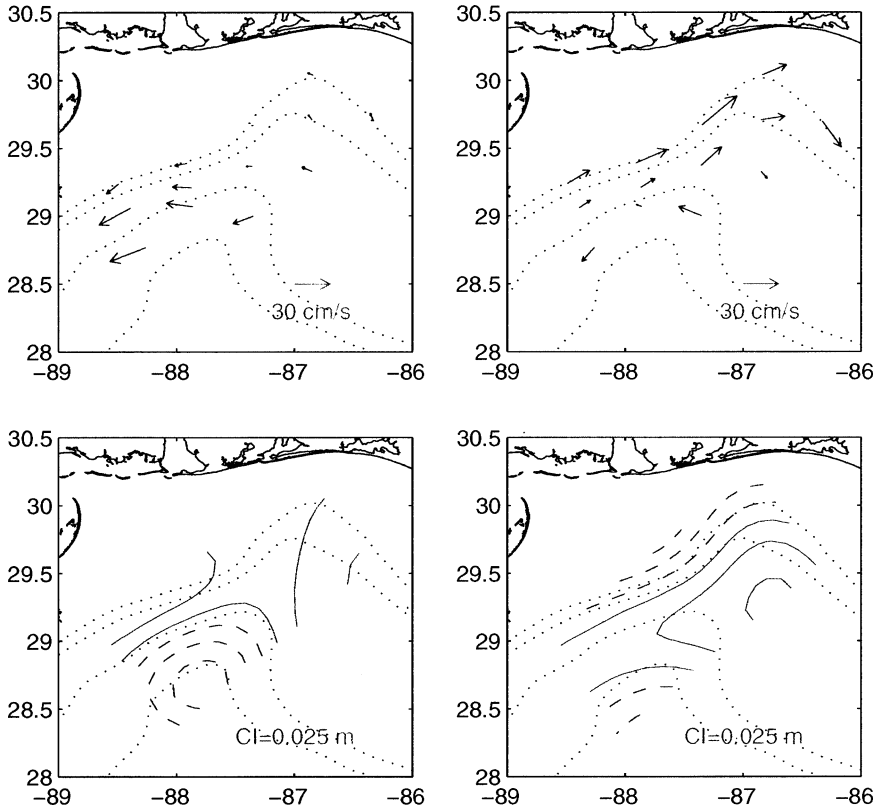

FIG. 2. (top) Currents and (bottom) geopotentials on (right) day 449 and (left) day 191 derived from objective analysis of moored current meters. The time is referenced to 1 Jan 1997.

daily averaged currents, and spatially mapped to produce daily surface geopotential distributions. The common procedure involves either multivariate functional fitting (e.g., Cho et al. 1998) or multivariate objective interpolation (MOI) (Bretherton et al. 1976). In this study, the universal co-kriging method (UCK) of Pedder (1989) (also see Gomia et al. 2001) is employed, which is a direct extension of MOI by allowing for the possibility of flow divergence. A velocity vector (u, v) can be decomposed into nondivergent (streamfunction) and divergent (velocity potential) components:

$$u = -\frac{\partial \psi}{\partial y} + \frac{\partial \chi}{\partial x}, \qquad v = \frac{\partial \psi}{\partial x} + \frac{\partial \chi}{\partial y}. \tag{1}$$

In MOI, only the streamfunction is used. In UCK, the spatial structures of streamfunction ψ and velocity potential χ are both optimally interpolated from observed currents. For example, the streamfunction can be expanded as

$$\psi(r_i) = \sum_k W^u_{ik} u(r_k) + W^v_{ik} v(r_k). \tag{2}$$

The summation is over all observations r_k with corresponding weights W^u and W^v. The velocity potential can be likewise expanded. The weights are determined by minimizing the data misfit following the standard least squares procedure (e.g., Daley 1993), and the solution matrix requires specification of the cross-covariance matrices, $\langle \psi_1 u_k \rangle$ and $\langle \psi_i v_k \rangle$, or equivalently, the covariance of $\langle \psi_i \psi_j \rangle$, $\langle \chi_i \chi_j \rangle$, and $\langle \psi_1 \chi_j \rangle$. In MOI, the autocorrelation functions are assumed to have a universal Gaussian (or other) functional shape. In UCK, in addition, ψ and χ are assumed uncorrelated and the geopotential is assumed to relate linearly to the streamfunction. The following parameters are used in the present analysis: horizontal scale length = 50 km; fractional divergence variance = 0.1; fractional geostrophic variance = 0.9. The results are not particularly sensitive to the chosen parameters. The analysis domain is 200 km × 100 km, aligned with the canyon axis, with a grid resolution of 10 km. The analysis yields daily maps of streamfunction, velocity potential, geopotential, and associated rotational, divergent, and geostrophic velocity fields.

In the model–data comparison, the focus will be on the geopotential. Figure 2 shows snapshots of the interpolated total velocity and geopotential on day 449 (25 March 1998) and day 191 (17 July 1997). The time origin is set at 1 January 1997. On day 449, the flow is concentrated at the foot of the canyon and appears to be part of a cyclonic eddy stalled against the canyon wall. In contrast, on day 191 the flow is concentrated on the head of the canyon and appears to be associated with an anticyclonic eddy overlying on the upper slope.

Also, the flow is unidirectional on day 449, but the flow direction is reversed at the foot of the canyon on day 191. At both times the velocity field is essentially geostrophic as indicated by the close association between the velocity and geopotential.

3. Satellite observations

Satellite altimeter data, archiving, validation, and interpretation of satellites oceanographic, (AVISO), are obtained from the French Space Agency. The data product was created by merging TOPEX/Poseidon (T/P) and *ERS-1* and *-2* altimeter measurements for the period between October 1992 and May 1998 (Ducet et al. 2000). The combined, intercalibrated altimeter data are interpolated in time and space using a global objective analysis. The length scale of the interpolation varies with latitudes, and is about 200 km at midlatitudes. The *e*-folding timescale is set at 10 days in the Tropics and 15 days elsewhere. The resulting satellite product has a spatial resolution of $0.25° \times 0.25°$ and is provided at 10-day intervals. The merged T/P + *ERS-1* and *-2* sea level anomaly maps provide reduced and more homogeneous mapping errors than either individual dataset, and thus, more realistic sea level and geostrophic velocity statistics.

It should be noted that satellite data consist of sea level anomalies as opposed to sea surface heights (SSH). Therefore, it is not possible to compare mean (over the 2-yr study period) currents between moored current meters and satellite data. The same problem also occurs in the data assimilation. However, the lack of a reference mean sea surface topography is resolved in the model by mapping satellite SLA into model's corresponding temperature anomalies (with respect to climatological mean temperatures; see below).

Ohlmann et al. (2001) compared surface currents derived from satellite SLA and drifters. Their results indicate that in the northeastern gulf, the two velocity estimates are comparable (correlation ~ 0.5) over the shelf edge (water depth > 200 m) and in the open water (water depth > 2000 m) but they are poorly correlated on the shelf (correlation ~ 0.2). We can make a similar comparison between moored current meter- and SLA-derived velocities for the DSC area. The current meter data are the actual daily velocities whereas the SLA-derived data are the gridded geostrophic velocities. Table 1 lists the correlations at the thirteen mooring locations for eastward, northward and principal-axis velocity components. The correlations are low ($\sim$0.2) for shelf (100 m) moorings and are modestly high (0.5 to 0.6) for shelfbreak and upper-slope moorings. These results agree well with those based on the surface drifters.

TABLE 1. Correlation coefficients between observed and satellite altimeter derived current velocities at each mooring location.

Mooring location	Eastward velocity	Northward velocity	Principal axes
A1	0.27	0.21	0.06
A2	0.35	0.32	0.13
A3	0.55	0.48	0.63
B1	0.37	−0.03	0.35
B2	0.44	0.04	0.55
B3	0.49	0.13	0.62
C1	0.18	0.22	0.22
C2	0.37	0.29	0.36
C3	0.54	0.46	0.57
D1	0.10	−0.02	0.16
D9	−0.10	−0.21	0.20
D2	0.06	−0.14	0.49
E1	0.30	−0.10	0.16

4. Model

a. Western North Atlantic model

The Princeton Ocean Model (Mellor 2002) is used in an orthogonal curvilinear grid system that covers the region west of 55°W in the western North Atlantic, including the Caribbean Sea and the Gulf of Mexico (Fig. 3; Oey and Lee 2002). Steady inflow and outflow transports are specified at 55°W (W. J. Schmitz, Jr., 2001, personal communication; see also Schmitz 1996). These transports determine the two-dimensional depth-integrated velocities at the boundary, and are meant to account for the large-scale transports (Svedrup + thermohaline) through 55°W. The three-dimensional velocity, temperature and salinity fields at the open boundary are calculated according to Oey and Chen (1992a). For example, the temperature and salinity fields are advected using one-sided difference scheme when flows are eastward (i.e., outflow), and are prescribed from the monthly temperature and salinity climatology (Levitus and Gelfeld 1992) when flows are westward. These open-boundary specifications also set the baroclinic structure, which in the present case is largely geostrophic through the thermal-wind balance. The prescribed open boundaries are sufficiently removed from the Gulf of Mexico that there is a free dynamical interaction between the Caribbean Sea and the gulf through the Yucatan Strait (Oey 1996).

POM uses the sigma transformation in the vertical. We use 25 sigma levels with finer resolution over the upper and lower 500–1000 m of the water column, so that LC, LCE, and bottom-trapped topographic Rossby waves (TRW) can be better resolved. The horizontal grid sizes vary from 5 km in the northern gulf including the DSC, 10 km in the vicinity of the LC, and 20 km in the southwestern corner of the gulf. The sigma-level pressure gradient error (Haney 1991) in the model is reduced by removing the basin-averaged density distribution (in z only) from the time-dependent density field before evaluating the pressure gradient terms (Mellor et al. 1998). Rigorous error evaluation during the course of integration is difficult. Nevertheless, a 1-yr test calculation using initially level density field with a small perturbation (amplitude $= 0.1$ kg m^{-3}, see Mellor et al. 1998) and zero forcing was conducted. The maximum current (the error) is <0.15 cm s^{-1}, which is negligible.

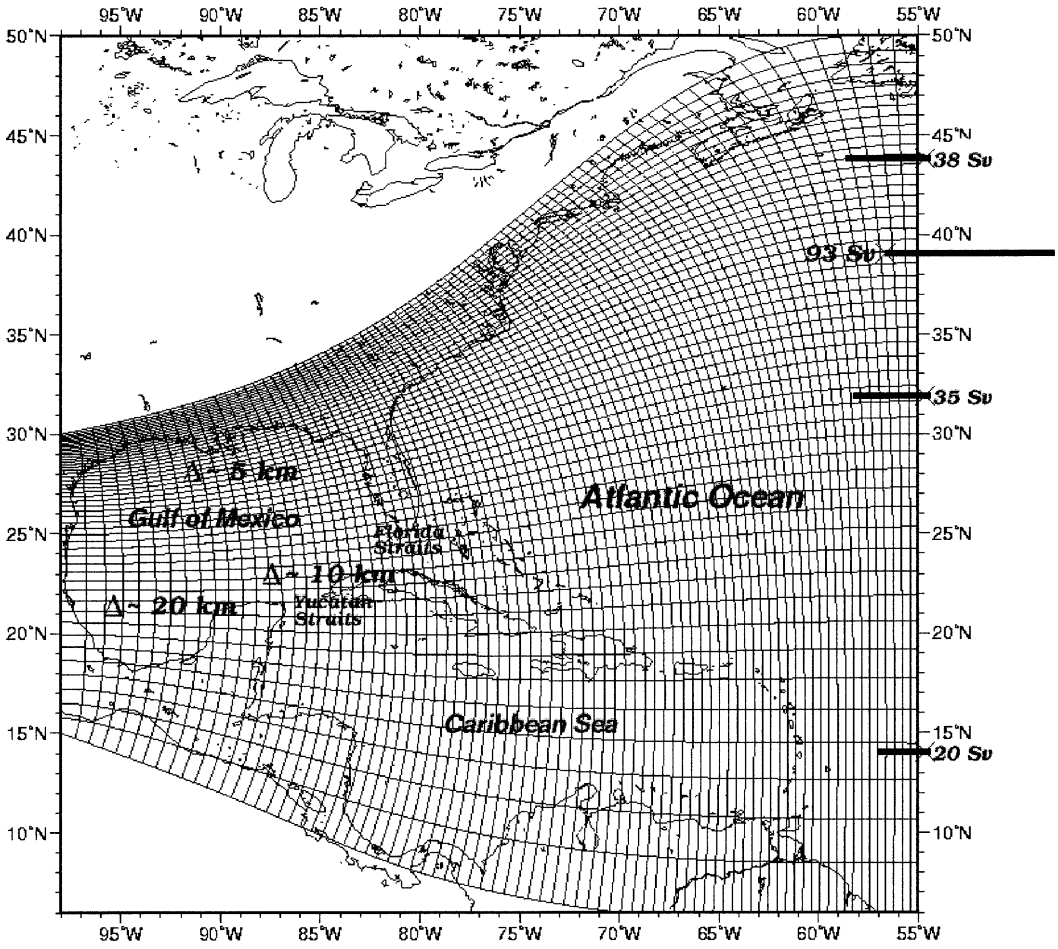

FIG. 3. North Atlantic Ocean model domain. The inflow and outflow transport profile is specified across 55°W as shown schematically. The model orthogonal curvilinear grid lines are shown every seventh grid point.

b. Embedded Gulf of Mexico model

The large-domain (western North Atlantic) model is expensive to run. A regional Gulf of Mexico model (e.g., Oey 1996), driven by inflow transports from the Cayman Sea and outflow through the Florida Strait, on the other hand, allows rapid model execution. However, inconsistent specifications of the inflow structure (such as the potential vorticity) may produce false information in the Gulf interior. This problem is handled by making the Cayman Sea inflow dynamically consistent with a Caribbean circulation deduced from the large-domain model. The requirement of outer- and inner-solution compatibility is met through ''embedding,'' in which both the outer and inner grids share an overlapped region where the two grids are exactly the same (based on Oey and Chen 1992b). Once the transports are computed from the outer model, the inner model utilizes the outer information and can be executed independently. This approach resolves the uncertainty in open-boundary treatments and allows efficient and rapid parametric sensitivity studies. L.-Y. Oey et al. (2002, unpublished manuscript) provides detailed description of the model formulation.

c. Satellite data assimilation

The satellite data are assimilated into the model following the methodology given in Mellor and Ezer (1991) and Ezer and Mellor (1994, 1997). The western North Atlantic Model is integrated without assimilation for 10 yr, forced by 6-hourly European Centre for Medium-Range Weather Forecast (ECMWF) wind and surface heat and salt flux; the latter is through relaxation to monthly climatological surface temperatures and salinities (T/S). The correlations between sea level anomaly and subsurface T/S are calculated from the model results. They are relatively high (>0.6) over a substantial portion of the gulf down to 500 m, but are low near the continental slope and rise (Fig. 4).

Given the satellite SLA, $\delta\eta_{sa}$, the model subsurface temperature anomaly δT is calculated as

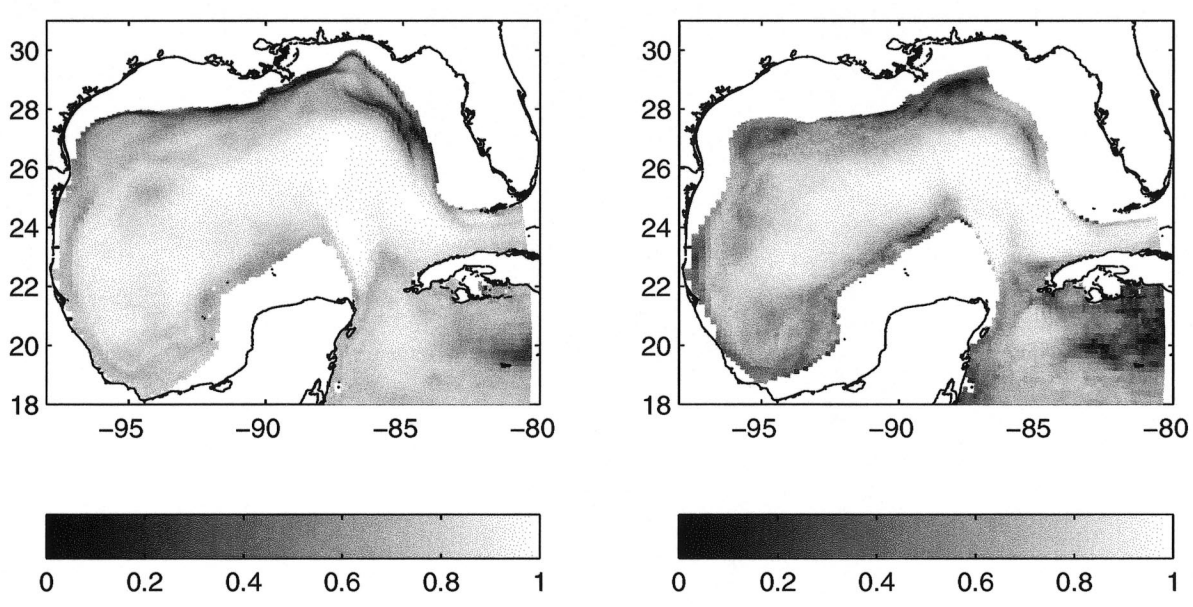

FIG. 4. Correlation coefficients between model-calculated sea level anomaly and temperatures at depths of (left) 100 and (right) 500 m.

$$\delta T(x, y, z, t) = F_T(x, y, z)\delta\eta_{sa}(x, y, t), \quad (3)$$

where the correlation factor is

$$F_T = \langle \delta T \delta\eta \rangle / \langle \delta\eta^2 \rangle, \quad (4a)$$

and the corresponding correlation coefficient is

$$C_T = \langle \delta T \delta\eta \rangle / (\langle \delta T^2 \rangle \langle \delta\eta^2 \rangle)^{1/2}. \quad (4b)$$

After each assimilation time step $\Delta t_A (=1$ day), the model temperature T is replaced by assimilated temperature T_A:

$$T_A = T + [2R_A C_T^2/(1 + 2R_A C_T^2 - C_T^2)](T_O - T), \quad (5)$$

where R_A is the ratio of Δt_A to the decorrelation timescale Δt_E of the model eddy field ($\approx$30 days), and T_O is the ''observed'' temperature inferred from satellite SLA, from (3):

$$T_O = \langle T \rangle + F_T \delta\eta_{\text{sa}}. \quad (6)$$

In (6) $\langle T \rangle = T_C$, the climatological mean temperature. The assimilation effect is such that in regions $T_A \approx T_O$ where the correlation is high, but $T_A \approx T$, where the correlation is small. Also, to minimize potential satellite errors near the coast, the SLA assimilation is restricted to regions where water depths are $>$500 m, thus excluding the shelves. A similar assimilation of SST is also carried out after (5), with the same Δt_A but with C_T and F_T replaced by the corresponding functions that use δ(SST) in place of $\delta\eta$ in (4). Weekly multichannel satellite SST maps, obtained from the Jet Propulsion Laboratory (JPL), are used for this purpose. The SST assimilation is applied to the entire region, over the shelves as well as deep waters. Sensitivity experiments indicate that the SSH and SST assimilations complement each other—the former is effective over the deep portions of the gulf while the latter is most effective over the shelves. We comment, however, that since the satellite does not resolve well the smaller-scale peripheral eddies (diameters $\approx$ 150 km and less), the assimilation is biased toward larger eddies, usually anticyclones. We are therefore more reliant on the model's intrinsic dynamics for small-scale physics.

In the Gulf of Mexico, the eddy activities are mainly associated with LCE. The LC typically stays south of 25°N along the west Florida Escarpment. However, about every 8–10 months, the LC extrudes northward and a LCE is shed and propagates west- or southwestward. Thus, high eddy variability is concentrated in a zonal band that marks the region of LCE influence. Figure 5 compares the rms (averaged over three years from 1997 through 1999) from the model and from satellite-derived SLA. As should be expected from a model experiment with data assimilation, both the shape and intensity of the model SLA agree well with those derived from satellite SLA. The model appears to be slightly more energetic, which is probably due to model's natural variability.

5. Comparison of model with observations

The model–data comparison focuses on the surface geopotentials and associated geostrophic currents. In

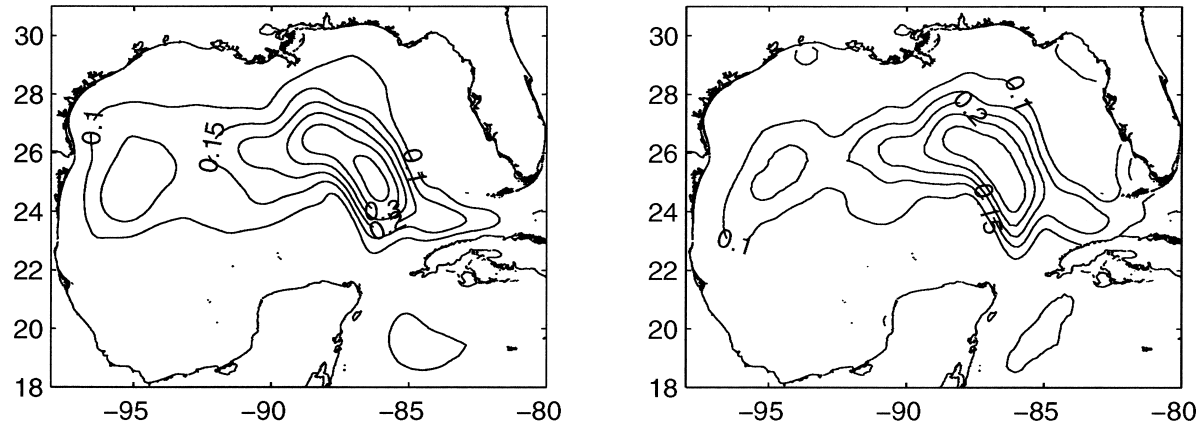

FIG. 5. Comparison of (left) model and (right) satellite-derived rms sea level anomaly (m).

general, the surface currents are much more energetic than in the deep (>200 m) water, and at low frequencies currents are dominated by their geostrophic component. Thus, it is useful to examine first the surface geopotential (without loss of generality). Also, the observed near-surface currents are from the measurements at 20-m depth. Near-surface vertical shears are mostly caused by friction (Ekman layer, for example), and will not contribute to the surface geopotential. It is more advantageous to consider surface geopotential in comparison between model and current meter and satellite observations.

The satellite product uses *e*-folding time of 15 days. To ensure all three datasets are compatible, model and observed velocity fluctuations are filtered with a cutoff period of 15 days. Figure 6 shows comparison between the original velocity, UCK-interpolated velocity, and 15-day filtered velocity. This example is for the eastward velocity component at B2. The UCK acts like a spatial filter. It retains the same frequency content but removes the small-scale variability that appears as ''spikes'' in the time series plot. The temporal filter removes the high-frequency variability generally associated with the wind forcing. The low-frequency (''eddy'') variance typically is about 75%–85% of the unfiltered variance, except at D1 where the ratio is about 50%. It should be noted that the spatial and temporal filters do not alter the spatial velocity structure. The leading empirical orthogonal function (EOF) modes derived from the original velocity, UCK interpolated velocity, and 15-day filtered velocity, are virtually identical.

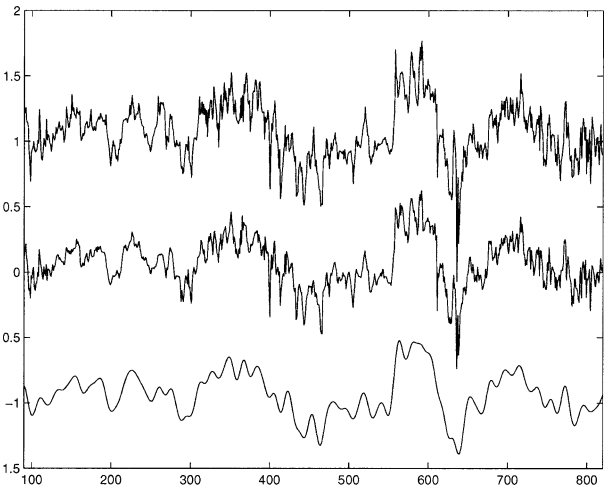

FIG. 6. Comparison of (top) original velocity time series with (middle) interpreted and (bottom) filtered velocity time series. The velocity record is the eastward velocity component at mooring B2 (the velocity scale is meters per second). Each time series plot is offset by 1 m s^{-1}. The time is referenced to 1 Jan 1997.

a. SVD analysis

Low-frequency eddy motions are not fully deterministic, and we should not normally expect to find high local (point-wise) correlations between model and observed currents. A useful approach in making model–data comparison is to explore the possibility that the model results may have retained comparable spatial and temporal patterns with the observed currents. The observed currents, model results, and satellite data are spatial time series with same data length (in time) but not (necessarily) same spatial domain. For any two spatial time series that are collocated at N grids, the correlation matrix contains N diagonal terms of local correlations, and $\sim N^2/2$ off-diagonal terms of cross correlations. Typically, $N \gg 1$, and the off-diagonal terms contain rich information about the spatial relationship between the two spatial time series.

The structure of the correlation matrix, including both the diagonal and off-diagonal terms, can be systematically reduced to identify coherent spatial patterns between the two spatial time series. Singular value de-

composition (SVD) is an effective technique to accomplish such purpose. Following Bretherton et al. (1992), the spatial vector time series $s(t)$ and $z(t)$, can be expanded in terms of a set of patterns (NS and NZ are the vector dimensions in $s(t)$ and $z(t)$:

$$s(t) \leftarrow \tilde{s}(t) = \sum_{k=1}^{\mathrm{NS}} a_k(t)p_k \tag{7a}$$

$$z(t) \leftarrow \tilde{z}(t) = \sum_{k=1}^{\mathrm{NZ}} b_k(t)q_k. \tag{7b}$$

The time series $a_k(t)$ and $b_k(t)$ are called the left and right expansion coefficients and the vectors p_k and q_k are the corresponding spatial patterns. It can be shown that if p_k and q_k are the kth left and right singular vectors of the covariance matrix $\mathbf{C}_{sz}$, the covariance between the kth left and right expansion coefficients, $\langle a_k b_k \rangle$, is equal to the corresponding kth singular value. The SVD expansion can be ordered such that the first mode corresponds to the largest singular value, and so on. The percentage of the covariance explained by the k mode, the squared covariance fraction (SCF), is

$$\mathrm{SCF}_k = \frac{\langle a_k b_k \rangle^2}{\|\mathbf{C}\|^2}, \tag{8}$$

where the squared Frobenius matrix norm is the total amount of squared covariance summed over all entries in $\mathbf{C}$:

$$\|\mathbf{C}\|^2 = \sum_{i=1}^{\mathrm{NS}} \sum_{j=1}^{\mathrm{NZ}} \mathbf{C}_{ij}^2. \tag{9}$$

Obviously, $\mathrm{SCF}_1 > \mathrm{SCF}_2$, and the first mode extracts most of the spatial covariance (as defined by the Frobenius matrix norm).

The composite principal component analysis (CPCA), which applies EOF analysis to the combined $s(t)$ and $z(t)$ spatial time series, can be an alternative to SVD. In general, if the coupled signals are similar to the dominant EOFs of the individual fields, there is little difference between SVD and CPCA. However, if the coupled signals are dissimilar from the EOFs but are still smooth in the sense that they project principally onto only the leading few modes of the individual fields, SVD may be superior to CPCA (Bretherton et al. 1992; Wallace et al. 1992). In the present case, the model and observation are not very similar (otherwise, the pointwise comparison will be adequate), and SVD seems to give better representation than CPCA. The SVD is being used widely in the climate research, which faces the same challenge as in the present study in trying to identify nondeterministic signals. For example, Lau and Weng (2001) used SVD to examine the relationship between the rainfall variability over China and global SST, and Robertson et al. (2000) used SVD to identify the influence of Atlantic SST on model simulated North Atlantic Oscillation.

b. Surface geostrophic currents

Model and observed mean currents and their corresponding variance (rms velocity) ellipses are shown in Fig. 7. Mean currents are eastward and their magnitudes are small ($\sim$5 cm s^{-1}) compared to the fluctuations ($\sim$15 cm s^{-1}). Both the means and variance ellipses tend to follow the bottom topography. The model mean currents are generally in good agreements with the observed currents, having the same general direction and comparable magnitude. However, the model means are much too strong ($>$10 cm s^{-1}) near the head of the canyon. In the model, this ''shelfbreak jet'' continues along the west Florida shelf. Similar jet feature was found in the previous nondata assimilated models of the west Florida shelf (Oey 1996; Hetland et al. 1999). While there was tentative evidence for a shelf-edge jet from surface drifter observations, the mooring data do not appear to support it. The model variances also agree well with the observed. The model ellipses are narrower than the observed, suggesting that the model currents are more strongly constrained by the bottom topography. Correlation coefficients (γ) between model and observed currents vary, ranging from low values of $<$0.2 to modestly high values of 0.5 (not shown).

We use SVD to extract patterns in model currents that are coherent with observed currents. In our convention the left data field is assigned to observed currents and the right data field is assigned to model currents. Each spatial time series consists of 2-yr velocity time series at 26 ''grids,'' that is, $N = \mathrm{NS} = \mathrm{NZ} = 26$, corresponding to the u and v at 13 mooring locations. (We count u and v as independent variables.) The 2-yr means are removed. There are 26 possible modes in the expansion of (7). The first mode alone, however, explains 96% of the covariance between observed and model currents (that is, $\mathrm{SCF}_1 = 0.96$), and the second mode explains 2%. The method captures almost the entire covariance structure in a single mode.

Figure 8 shows the first and second expansion coefficients (''modes'') of observed (left) and model (right) currents; the modal amplitudes are normalized. The first mode accounts for 49% and 59% respectively of the observed and model variances. In both modes the dominant fluctuations have long periods of about 100 to 200 days. The first modes of observed and model currents are similar with $\gamma = 0.65$. In the first mode of observed currents, the strong depression (cyclonic circulation) around day 640 was caused by Hurricane Georges, which passed over DSC on 29 September 1998. The model forcing, which is based on the ECMWF wind, underestimated the hurricane strength, and the model result did not produce the strong response. Figure 9 shows the first and second spatial patterns of observed and model currents. The mode-1 spatial patterns of observed and model currents are comparable in that both indicate a single-eddy structure located at the foot of the canyon. (The term ''eddy'' is

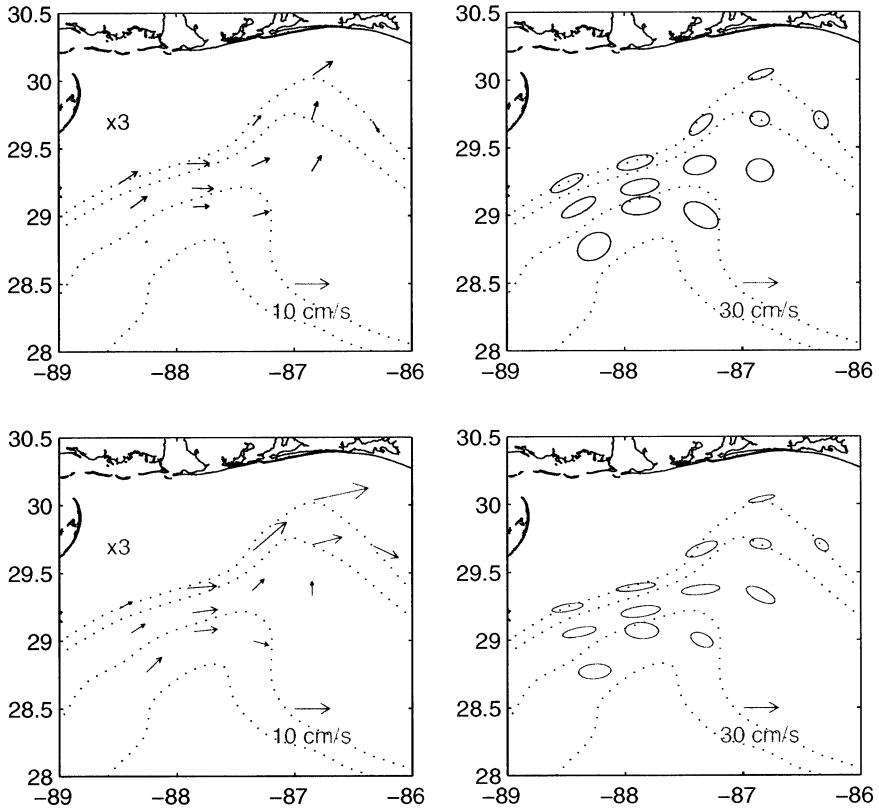

FIG. 7. (left) Mean currents and (right) variances at mooring locations from (top) observations and (bottom) model. Note that the velocity scale for means is 3 times as large. Dotted are isobaths: 2000, 1000, 200, and 100 m.

used here to describe unidirectional flows over the shelf edge. Since the geostrophic flow is nondivergent, the unidirectional flow must somehow veer around the shelf edge, turning either cyclonic or anticyclonic.) Also, both the observed and model eddies appear to be ''blocked'' by the steep canyon wall. This shows that the model results contain a high degree of reality, as both the model and observed currents indicate similar spatial and temporal structures for the dominant fluctuations. The mode-2 spatial pattern consists of an isolated eddy at the head of the canyon, and the correlation (γ) between observed and model second modes is 0.51. The fractional variances explained by mode 2 are 10% and 12%, respectively, of the observed and model currents.

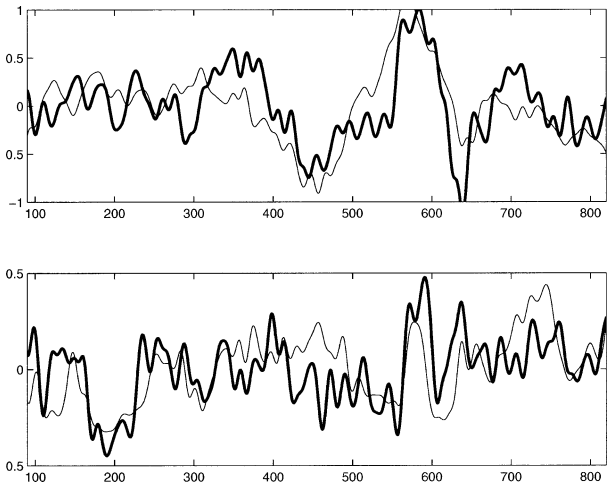

FIG. 8. (top) First and (bottom) second modes of observed (heavy lines) and model (light lines) currents. The time is referenced to 1 Jan 1997.

The observed currents also are compared with the geostrophic currents derived from satellite SLA. The $0.25° \times 0.25°$ SLA data are first mapped onto the 10 km $\times$ 10 km analysis grid, and SVD is used to find coupled patterns between observed and satellite-derived currents. Figure 10 shows the first and second modes of observed and satellite-derived currents. The first mode of observed currents is virtually identical to the one derived earlier (cf. Fig. 8). The first modes of observed and satellite-derived currents are well correlated with $\gamma = 0.83$. The satellite SLA also underestimated the hurricane response (day 640), which can be attributed to the low temporal and spatial resolution in satellite remote sensing. The second modes of observed and satellite-derived currents also are highly coherent ($\gamma = 0.71$). Obviously, satellite SLA is able to retain accurate temporal information.

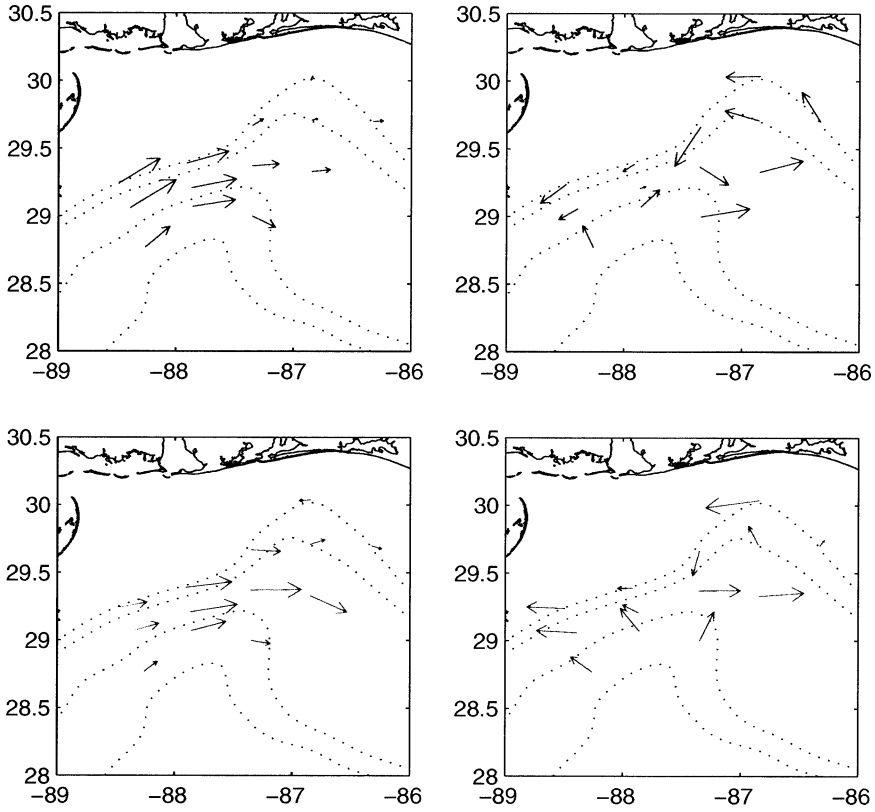

FIG. 9. (left) First and (right) second spatial patterns of (top) observed and (bottom) model currents. The velocity scale is arbitrary. Dotted are isobaths: 2000, 1000, 200, and 100 m.

The first spatial pattern (Fig. 11) of observed currents is the same as in the earlier case, showing a single eddy confined to the deeper part of the canyon (cf. Fig. 9). The first spatial pattern of satellite-derived currents also indicates a single eddy; however, the eddy seems to penetrate well onto the head of the canyon. In other words, the satellite-derived currents are less constrained by the steep canyon wall. This is expected since satellite SLA is spatially smoothed with a length scale of 200 km. Indeed, it is most surprising that the satellite-derived currents can resolve the eddy structure. The second spatial pattern of observed currents suggests two counter rotating eddies splitting roughly at the center of the canyon, one at the head of the canyon and the other at the foot. The mode-2 velocity pattern of observed currents again seems to be guided by the topography. The second spatial pattern of satellite-derived currents also reveals an eddy pair, and again its velocity structure seems to show more cross-slope motion.

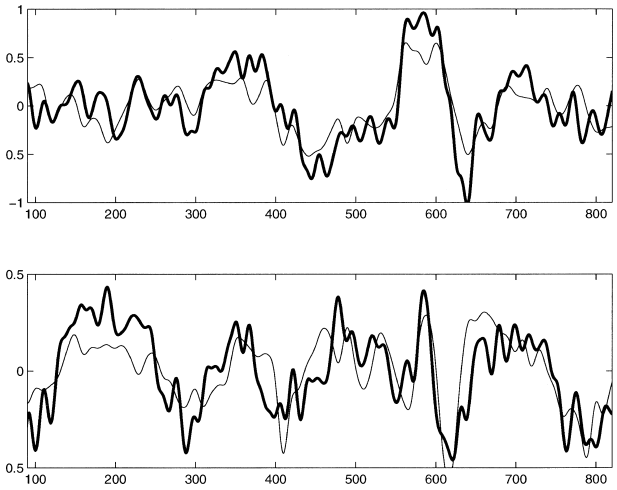

FIG. 10. (top) First and (bottom) second modes of observed (heavy lines) and satellite-derived (light lines) currents. The time is referenced to 1 Jan 1997.

The first mode explains 87% of the covariance between observed and satellite-derived currents, and accounts for 48% and 40% respectively of the observed and satellite-derived variances. The second mode explains 10% of the covariance, and accounts for 16% and 18% respectively of the observed and satellite-derived velocity variances. The first mode is the dominant fluctuation. The second mode, whose temporal and spatial structures are quite different from the second mode derived between observed and model currents, also seems to be quite meaningful. This is supported by the fact that the first two EOF modes of observed currents are almost identical to the first two modes of observed currents of the SVD analysis.

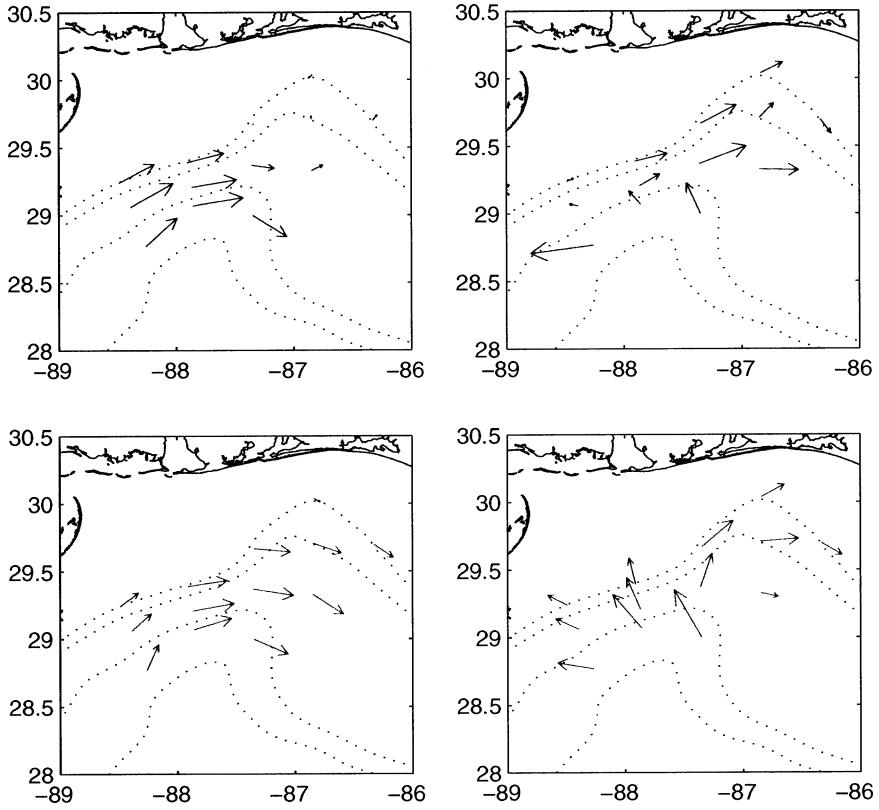

FIG. 11. (left) First and (right) second spatial patterns of (top) observed and (bottom) satellite-derived currents. The velocity scale is arbitrary. Dotted are isobaths: 2000, 1000, 200, and 100 m.

We can take advantage of the larger spatial coverage of satellite SLA to associate the eddy features to the open ocean influence. We calculate the regression of SLA time series at each grid point with the first and second SVD modes of observed currents. Figure 12 shows the correlation coefficient maps for the first and second modes. The mode-1 correlation map indicates a single eddy centered at the foot of the canyon and the mode-2 correlation map shows the eddy pair. For the first mode, interestingly, the entire shelf water also seems to respond to the single-eddy event. (The high negative-correlation shown in Fig. 12 extends to both

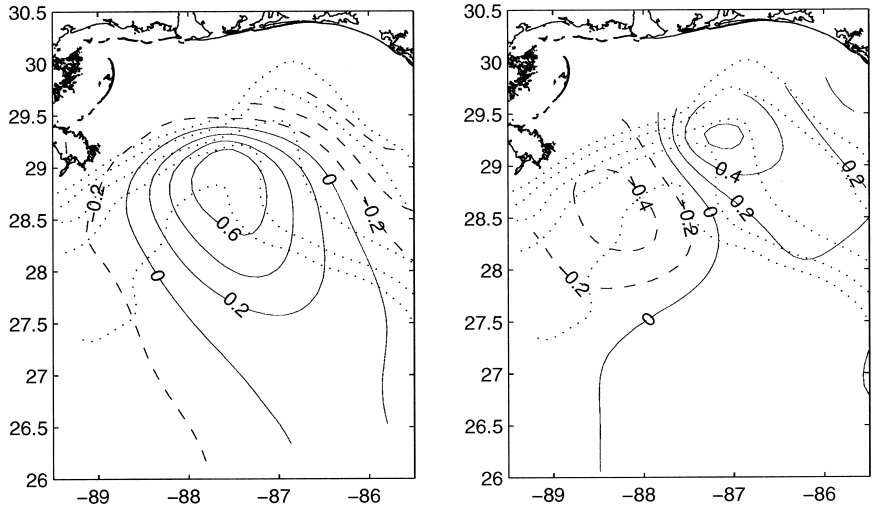

FIG. 12. Correlation coefficients of satellite sea level anomaly with (left) first and (right) second modes of observed currents. Dotted are isobaths: 2000, 1000, 500, 200, and 100 m.

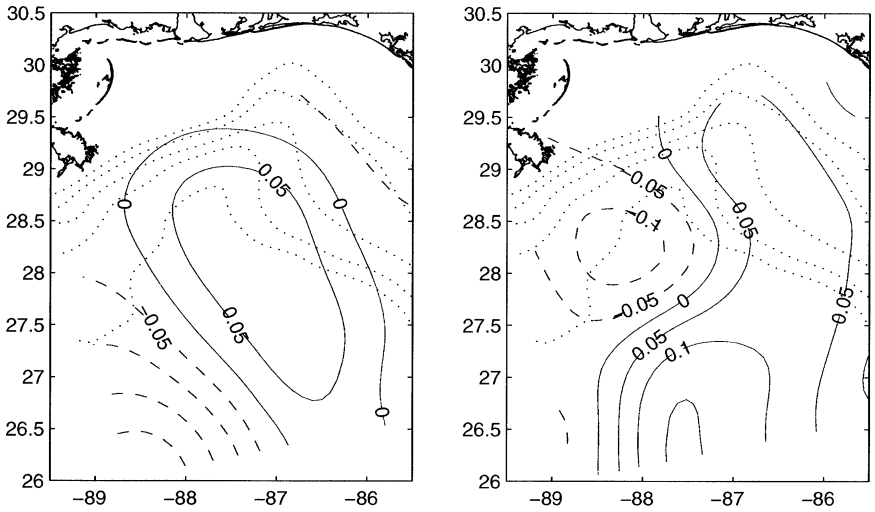

FIG. 13. Regression coefficients of satellite sea level anomaly with (left) first and (right) second observed modes. Dotted are isobaths: 2000, 1000, 500, 200, and 100 m.

the Mississippi–Alabama shelf and the southern west Florida shelf). The shelf sea level would rise when a cyclonic eddy is present in the DSC and fall when there is an anticyclonic eddy. For the second mode, the response is confined entirely to the shelf region.

Figure 13 shows the regression coefficient maps, which describe the spatial patterns associated with the SVD modes. The mode-1 eddy is related to a large and opposite fluctuation in the open ocean. This result indicates that the cyclonic eddy in the DSC is associated with the LC crest and the anticyclonic eddy is with the LC trough. For mode-2, the eddy is connected to a large fluctuation (of the same sign) in the open ocean, suggesting that the anticyclonic (cyclonic) eddy over the head of the canyon is associated with intrusion of the LC crest (trough). Examination of the two-year satellite SLA record indicates that the LC crest is present in the northeastern Gulf when the LC extrudes northward and the LC trough is present in the northeastern Gulf when the LC is at its normal southern location. The LC crest can be either associated with the LC or the detached LCE. The LC trough often is the remnant of the cyclone(s) that ''cut across the LC in the vicinity of 26°N, 87°W'' when a LCE is shed, as was noted by Oey (1996).

It is instructive to compare regression coefficient patterns with specific eddy events. Figure 14 shows satellite SLA snapshots on day 449 and day 191, corresponding to the negative phase of mode 1 and positive phase of mode 2 (cf. Fig. 10). Both periods correspond to extreme

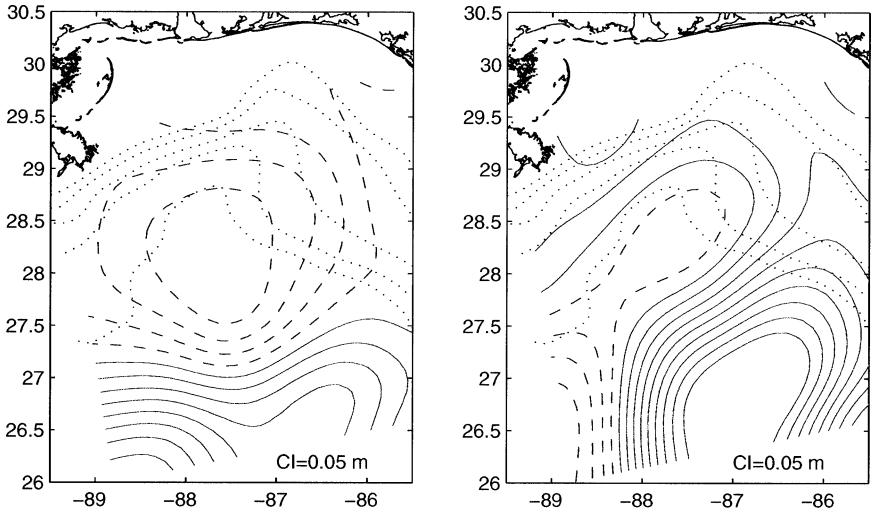

FIG. 14. Satellite sea level anomaly showing (left) a cyclonic eddy on Day 449 and (right) an LC intrusion on Day 191 (m). Dotted are isobaths: 2000, 1000, 500, 200, and 100 m. The time is referenced to 1 Jan 1997.

northward extensions of the LC/LCE. On day 449, a large cyclonic eddy is situated over the DSC. This cyclonic eddy can be followed traveling clockwise around the periphery of the LCE, at the time when the LCE is about to separate from the LC. (The edge of the LCE is indicated by large positive sea level anomaly in Fig. 14.) The SLA pattern of combined cyclonic eddy and LC crest is similar to the mode-1 regression coefficient. On day 191, the LC crest (indicated by large positive sea level anomaly) seems to slip over the west Florida shelf, and a cyclonic eddy is squeezed against the Alabama–Mississippi shelf. This pattern resembles the mode-2 regression coefficient. It is also interesting to compare satellite SLA pattern with geopotential surface derived from the moored current meters (cf. Fig. 2). While satellite SLA patterns lack the details (especially near the head of the canyon), they certainly capture the major features revealed in the moored current meter data.

6. Conclusions

Application of SVD analysis to the 2-yr observed and satellite-derived near-surface currents in DSC reveals two dominant modes of low frequency (''eddy'') fluctuations. Mode 1 consists of a single eddy trapped near the foot of the canyon, and mode 2 displays an eddy pair with counterrotating eddies at both ends of the canyon. Satellite SLA is consistent with the surface geopotential calculated from the observed currents, in the sense that it contains both modes. It is expected that satellite SLA is able to reproduce the first mode because satellite data are of good quality over the deep part of the Gulf. The presence of the second mode in satellite SLA is surprising. Despite the poor local correlations between satellite-derived and observed currents, satellite SLA somehow retains the coherent spatial patterns. This suggests the possibility of assimilating altimetry measurements, which will have major impacts on coastal ocean prediction experiments in the shelf and slope region.

The dominant mode-1 fluctuations are associated with both cyclonic and anticyclonic eddies. The cold cyclonic eddy (LC frontal eddy) has been well documented. In contrast, the anticyclonic eddy remains rather obscure. Wiseman and Dinnel (1988) found frequent presence of warm water and associated strong eastward currents on the Mississippi–Alabama shelf. Typically, those events were not associated with the deep northward extension of LC or LCE. We suggest that those warm intrusions were associated with the mode-1 anticyclonic eddy, which according to our analysis, is often present in this region when the LC is at its normal southern position. Ohlmann et al. (2001) also gave an example of an anticyclonic eddy from drifter trajectories and satellite SLA. The eddy was found around 22 August 1998 (day 599), corresponding to the time of a large positive (anticyclonic) mode-1 (cf. Fig. 10). Major LC intrusion on the west Florida shelf is even less documented. The LC frontal tracings given in Fratantoni et al. (1998) showed some instances when warm LC waters intruded along the west Florida shelf/slope, separated from a newly shed LCE farther west by a pool of cooler water. Their SST images are reminiscent of the mode-2 pattern.

The model simulation includes assimilation of both SLA and SST. The model means and current ellipses agree fairly well with the observations. The model currents contain realistic single-eddy structure that accounts for about half of the total velocity variance. Moreover, the model currents, unlike the corresponding satellite-derived currents, are constrained by the steep shelf/slope topography. This is encouraging since a principal benefit of employing data assimilation is to supplement partial observations with model dynamics. The model currents, however, do not agree as well as the satellite-derived currents. This suggests that our data assimilation scheme has not taken full advantage of the satellite information. One may relax, for example, the (arbitrary) constraint we imposed on assimilating the satellite SSH only in regions where the water depths $>$ 500 m. In other words, we may try to also assimilate satellite SLA over the shelf. A more serious shortcoming is that the degree of data nudging in (3) is determined by precomputed correlations between model sea level anomaly and subsurface temperatures. Unfortunately, the correlations are low over the northern gulf slope/rise (Fig. 3), and the data assimilation has little direct impact in the DSC. To improve the pre-computed correlations, the model will need to generate more realistic LC frontal eddy in the eastern gulf. Alternatively, it may be advantageous to use empirically derived correlations between SSH and subsurface temperatures.

Acknowledgments. We are grateful to supports by NAVOCEANO and ONR (DPW and LYO). The data collection and model development were supported by grants from the Minerals Management Service, Gulf of Mexico OCS Region.

REFERENCES

Bretherton, C. S., C. Smith, and J. M. Wallace, 1992: An intercomparison of methods for finding coupled patterns in climate data. *J. Climate*, **5,** 541–560.

Bretherton, F. P., R. E. Davis, and C. B. Fandry, 1976: A technique for objective analysis and design of oceanographic experiments applied to MODE-73. *Deep-Sea Res.,* **23,** 559–582.

Cho, K. R., R. O. Reid, and W. D. Nowlin, 1998: Objectively mapped stream function fields on the Texas–Louisiana shelf based on 32 months of moored current meter data. *J. Geophys. Res.,* **103,** 10 377–10 390.

Daley, R., 1993: *Atmospheric Data Analysis.* Cambridge University Press, 455 pp.

Ducet, N., P. Y. Le Tron, and G. Reverdin, 2000: Global high-resolution mapping of ocean circulation from TOPEX/Poseidon and ERS-1 and -2. *J. Geophys. Res.,* **105,** 19 477–19 498.

Ezer, T., and G. L. Mellor, 1994: Continuous assimilation of Geosat altimeter data into a three-dimensional primitive equation Gulf Stream model. *J. Phys. Oceanogr.,* **24,** 832–847.

——, and ——, 1997: Data assimilation experiments in the Gulf Stream region: How useful are satellite-derived surface data for nowcasting the subsurface fields? *J. Atmos. Oceanic Technol.,* **14,** 1379–1391.

Fratantoni, P. S., T. N. Lee, G. P. Podesta, and F. Muller-Karger, 1998: The influence of Loop Current perturbations on the formation and evolution of Tortugas eddies in the southern Strait of Florida. *J. Geophys. Res.,* **103,** 24 759–24 799.

Gomia, D., S. Ruiz, and M. A. Pedder, 2001: Diagnostic analysis of the 3D ageostrophic circulation from a multivariate spatial interpolation of CTD and ADCP data. *Deep-Sea Res.,* **48,** 269–295.

Haney, R. L., 1991: On the pressure gradient force over steep topography in sigma coordinate ocean models. *J. Phys. Oceanogr.,* **21,** 610–619.

Hetland, R., Y. Hsueh, R. R. Laben, and P. P. Niiler, 1999: A Loop Current induced jet along the edge of the west Florida shelf. *Geophys. Res. Lett.,* **26,** 2239–2242.

Huh, O. K., W. J. Wiseman Jr., and L. J. Rouse Jr., 1981: Intrusion of Loop Current water onto the West Florida continental shelf. *J. Geophys. Res.,* **86,** 4186–4192.

Lau, K. M., and H. Y. Weng, 2001: Coherent modes of global SST and summer rainfall over China: An assessment of the regional impacts of the 1997–98 El Niño. *J. Climate,* **14,** 1294–1308.

Levitus, S., and R. I. Gelfeld, 1992: NODC inventory of physical oceanographic profiles. Key to Oceanographic Records Doc. 18, NODC, Washington DC, 36 pp.

Li, Z., and R. H. Weisberg, 1999: West Florida shelf response to upwelling favorable wind forcing: Kinematics. *J. Geophys. Res.,* **104,** 13 507–13 527.

Mellor, G. L., 2002: User's guide for a three-dimensional, primitive equation, numerical ocean model (July 2002 version). Program in Atmospheric and Oceanic Sciences, Princeton University, 42 pp. [Available online at http://www.aos.princeton.edu/WWWPUBLIC/htdocs.pom/PubOnLine/POL.html.]

——, and T. Ezer, 1991: A Gulf Stream model and an altimetry assimilation scheme. *J. Geophys. Res.,* **96,** 8779–8795.

——, L.-Y. Oey, and T. Ezer, 1998: Sigma coordinate pressure gradient errors and the seamount problem. *J. Atmos. Oceanic Technol.,* **15,** 1122–1131.

Oey, L.-Y., 1996: Simulation of mesoscale variability in the Gulf of Mexico. *J. Phys. Oceanogr.,* **26,** 145–175.

——, and P. Chen, 1992a: A model simulation of circulation in the northeast Atlantic shelves and seas. *J. Geophys. Res.,* **97,** 20 087–20 115.

——, and ——, 1992b: A nested-grid ocean model. *J. Geophys. Res.,* **97,** 20 063–20 086.

——, and H. C. Lee, 2002: Deep eddy energy and topographic Rossby waves in the Gulf of Mexico. *J. Phys. Oceanogr.,* **32,** 3499–3527.

Ohlmann, J. C., P. P. Niiler, C. A. Fox, and R. R. Leben, 2001: Eddy energy and shelf interactions in the Gulf of Mexico. *J. Geophys. Res.,* **106,** 2605–2620.

Pedder, M. A., 1989: Limited area kinematic analysis by a multivariate statistical interpolation method. *Mon. Wea. Rev.,* **117,** 1695–1708.

Robertson, A. W., C. R. Mechoso, and Y. J. Kim, 2000: The influence of Atlantic sea surface temperature anomalies on the North Atlantic oscillation. *J. Climate,* **13,** 122–138.

SAIC, 2000: DeSoto Canyon eddy intrusion study. Draft Final Tech. Rep., MMS Contract 1435-01-96-CT-30825, 265 pp. [Available from SAIC, 615 Oberlin Rd., Suite 300, Raleigh, NC 27605.]

Schmitz, W. J., Jr., 1996: On the World Ocean circulation. Vol. I: Some global features/North Atlantic circulation. WHOI Tech. Rep. WHOI-96-03, 141 pp.

Vukovich, F. M., 1988: On the formation of elongated cold perturbations off the Dry Tortugas. *J. Phys. Oceanogr.,* **18,** 1051–1059.

——, and G. A. Maul, 1985: Cyclonic eddies in the eastern Gulf of Mexico. *J. Phys. Oceanogr.,* **15,** 105–117.

——, B. W. Crissman, M. Bushnell, and W. J. King, 1979: Some aspects of the oceanography of the Gulf of Mexico using satellite and in-situ data. *J. Geophys. Res.,* **84,** 7749–7768.

Wallace, J. M., C. Smith, and C. S. Bretherton, 1992: Singular value decomposition of wintertime sea surface temperature and 500-mb height anomalies. *J. Climate,* **5,** 561–576.

Wiseman, W. J., Jr., and S. P. Dinnel, 1988: Shelf currents near the mouth of the Mississippi River. *J. Phys. Oceanogr.,* **18,** 1287–1291.

Yuan, D., 2002: A numerical study of barotropically forced intrusion in Desoto Canyon. *J. Geophys. Res.,* **107,** 2.1–2.5.